ACTIVE CHARGING CONTROL AND TETHERS

Juan R. SANMARTIN
Universidad Politécnica de Madrid

ABSTRACT : *Electron collection by a bare tether and electron collection and ejection by a plasma contactor are analysed. Charge exchange is presented from an unified viewpoint, based on the Orbital Motion Limited current as a current gauge, and on graphs for* Φ *versus* $\Phi_P R^2/r^2$ [$\Phi(r)$ *is potential field,* Φ_P *and* R *are bias and radius of electrode, respectively*]. *A recent application to the International Space Station is discussed.*

RÉSUMÉ : On analyse contacteurs de plasma pour collecter ou éjecter des electrons, and amarres spatiales non-enrobées ('bare tethers') comme collecteurs. On présente échange de charge selon un point de vue unifié, basé sur le courant 'Orbital Motion Limited' comme jauge de courants, et sur le graphique Φ - $\Phi_P R^2/r^2$ [$\Phi(r)$ est champ potentiel, Φ_P et R sont potentiel et rayon de l'électrode, respectivement]. On décrit une récente application à la Station Spatiale Internationale.

1 - INTRODUCTION

Proper circuitry bias can make a Langmuir probe to draw no net current from a laboratory plasma. Usually conditions can be taken as isotropic, an electrically floating probe then satisfying a local relation: it draws net current nowhere on the probe surface, which keeps equipotential. One electron will leak out for each electron incident at any point on the probe because impacting ions carry an electron away in leaving as neutrals.

Conductors orbiting in space behave quite differently. They naturally float electrically, but anisotropy effects are ubiquitous. In LEO orbit, spacecraft (S/C) speed U_{sat} is hypersonic as regards (mainly oxygen) ions, resulting in ram and wake effects with current collection non-uniform over the probe surface. Also, when the S/C is not in eclipse, electron photoemission makes sunlit surfaces to be more positive, and collect net negative current from the ionosphere, the opposite holding for surfaces in the shade. All this results in permanent currents and ohmic voltage drops across a S/C.

The geomagnetic field B_0 makes the electron flow anisotropic too. Often, however, floating bias is negative and logarithmically large against the electron temperature T_e; with electrons in near (Boltzmann) equilibrium, directional effects come out to be weak. On the other hand, the motional electric field $\overline{U}_{sat} \wedge \overline{B}_0$ results in induced bias of order of 0.1 V/m in the S/C frame. Since T_e is about 0.1 eV, a typical floating S/C may sustain a substantial nonuniformity in bias.

Long, thin bodies such as tethers (length $L >>$ radius R) are extreme examples of effective motionally induced bias. Thin bodies range from the tin and copper dipoles placed in orbit at 3000 km heights forty years ago ($L \sim 10$ cm), to antennas ($L \sim 30$ m), to tethers ($L \sim 10$ km). For electrically floating bare tethers, which have been suggested as optimum electron-beam sources [1], full bias is much greater than the ion ram energy (~ 5 eV for oxygen ions); a fraction $(m_e/m_i)^{1/3} \approx 0.03$ of tether length then collects just electrons, which leak out over the remaining segment. For the small dipoles and for antennas, on the other hand, bias is everywhere negative, with net electron current at one end and net ion current at the other [2].

As a S/C moves in orbit its floating state will vary quasisteadily following changes in ambient conditions. Occasionally, however, sudden events (say, e-beam or electric-thruster firing) will violently disturb the near-equilibrium, taking rapidly the S/C to a new floating condition; active charge control through plasma contactors may be required to avoid extreme floating states. Contactors are being used to mitigate danger of arcing in the International Space Station (ISS), which has a 160 V primary power-generation system [3].

It has been suggested that a (non-floating) bare tether used in power generation, deorbiting or thrust, may efficiently collect electrons over some anodic segment [4]. Bare tethers have been shown more efficient than passive end-body electron collectors [5], [6]. However, the bare tether, while doing away with the need for anodic contactor, will require some active cathode that allows it not to float. Electron collection by tethers and electron collection or emission by plasma contactors are discussed in Secs. 2 and 3 from certain unified point of view. In Sec. 4 a recent application of both plasma contactors and bare tethers in the ISS is discussed.

2 - CHARGE COLLECTION BY ELECTRODYNAMIC TETHERS

2.1 - WIRE TETHERS

A bare tether collects current as a cylindrical Langmuir probe. Although bias varies along its length, a typical ratio length/thickness is of order 10^6, bare tethers collecting current per unit length as if uniformly biased at the local value. The electron current I to a probe at rest in a collisionless, unmagnetized, Maxwellian plasma of density N_∞ and temperatures T_e and T_i, may be written as

$$I = I_{th} \times \text{a function of } e\Phi_P/kT_e,\ R/\lambda_{De},\ T_i/T_e, \tag{1}$$

where $I_{th} \equiv 2\pi RL \times eN_\infty \times \sqrt{kT_e/2\pi m_e}$ is the random current, λ_{De} is Debye length, and R, L, and Φ_P are probe radius, length, and voltage bias. In general, determinining electron trajectories to obtain the collected current I requires solving Poisson's equation for $\Phi(r)$,

$$\frac{\lambda_{Di}^2}{r}\frac{d}{dr}r\frac{d}{dr}\left(\frac{e\Phi}{kT_i}\right) = \frac{N_e}{N_\infty} - \frac{N_i}{N_\infty}, \tag{2}$$

with boundary conditions $\Phi = \Phi_P > 0$ at $r = R$, $\Phi \to 0$ as $r \to \infty$. The theory of highly positive cylindrical probes has been fairly advanced recently [7]-[9].

Both the electric field $-\nabla\Phi$ and the probe acting as a sink of particles affect densities N_e and N_i, and thus $\Phi(r)$ itself. For $e\Phi_P >> kT_i$, kT_e values of interest, the repelled-particle density N_i follows the Boltzmann law

$$N_i \approx N_\infty exp(-e\Phi/kT_i) \tag{3}$$

except near the probe, where N_i is fully negligible anyway. As regards N_e, since all electrons originate at infinity and the Vlasov equation conserves the distribution function $f_e(\bar{r},\bar{v})$ along trajectories, we have $f_e(\bar{r},\bar{v}) = f_{eM}(v_\infty)$ (undisturbed Maxwellian) if the $\bar{r},\bar{v}$ trajectory traced back in time reaches infinity, and $f_e(\bar{r},\bar{v}) = 0$ otherwise. Energy is also conserved and f_{eM} is isotropic, values for $r, \bar{v}$ thus determining the value of f_{eM} in terms of the local potential $\Phi(r)$. The density $N_e(r)$ may then be expressed as an integral of f_{eM} over axial velocity v_z and (allowed ranges of) angular momentum J and energy E in the perpendicular plane, which are all three conserved,

$$J \equiv m_e r v_\theta, \qquad E \equiv \frac{m_e}{2} v_r^2 + \frac{m_e}{2} v_\theta^2 - e\Phi. \tag{4a, b}$$

A trivial v_z integration, and a change of variables $v_r, v_\theta \to E, J$, yields

$$N_e = N_\infty \iint \frac{\exp(-E/kT_e)\,dE\,dJ}{2\pi\, kT_e \sqrt{J_r^2(E) - J^2}}, \tag{5}$$

where we defined

$$J_r^2(E) \equiv 2m_e r^2 [E + e\Phi(r)]. \tag{6}$$

The E-integral only covers positive values and must be carried out once for $v_r < 0$ (incoming electrons) and again for $v_r > 0$ (electrons that have turned outwards at a radius between r and R); the J-integral is made to cover just positive values by writing $dJ \to 2dJ$. The J-range of integration in Eq.(5) is both E- and r-dependent. Extreme values $J = 0$ and $J = J_r(E)$ correspond to zero azimuthal and radial velocities respectively; the obvious condition $J^2 \le J_r^2(E)$ in (5) may be read as $E > U_r(J^2) \equiv -e\Phi(r) + J^2/2m_e r^2$ (radial effective potential energy). Angular momentum may be further limited, however:

i) For an incoming electron of energy $E > 0$ to actually reach r, $v_{r'}^2$ must have been positive throughout the entire range $r < r' < \infty$. Using (6) and (4a) in Eq.(4b),

$$m_e^2 r^2 v_r^2 = J_r^2(E) - J^2,$$

and using J-conservation, its range of integration at that energy will clearly be

$$0 < J < J_r^*(E) \equiv minimum\ \{ J_{r'}(E)\ ;\ r \le r' < \infty \}. \tag{7}$$

In general, the minimum occurs at a different r' at each energy E. In case we have $J_r^*(E) < J_r(E)$, electrons in the range $J_r^*(E) < J < J_r(E)$, for which v_r^2 would actually be positive, never reach r and must thus be excluded from the integral in (5). Corresponding inward trajectories, if traced back in time, turn around at radii between r and the (larger) radius where the minimum in (7) occurs, and are therefore unpopulated: one says that there is a $U_r(J^2)$ barrier for r at energy E.

ii) For an E-electron outgoing at r the J-range of integration will be

$$J_R^*(E) < J < J_r^*(E),$$

electrons in the range $0 < J < J_R^*(E)$ having disappeared at the probe. Equation (5) may now be written as

$$\frac{N_e}{N_\infty} = \int_0^\infty \frac{dE}{\pi kT_e} \exp\left(\frac{-E}{kT_e}\right)\left[2\sin^{-1}\frac{J_r^*(E)}{J_r(E)} - \sin^{-1}\frac{J_R^*(E)}{J_r(E)}\right]. \tag{8}$$

Note that, through its dependence on $J_r^*(E)$ [and $J_R^*(E)$], the density N_e is a functional of $\Phi(r)$, and thus cannot be known for use in solving Eq.(2) for $\Phi(r)$ before the potential itself is found; this may result in a complex, iterative numerical solution of Poisson's equation.

The current is easily found to be

$$\frac{I}{I_{th}} = \frac{2}{\sqrt{\pi}} \int_0^\infty \frac{dE}{kT_e} \exp\left(\frac{-E}{kT_e}\right) \frac{J_R^*(E)}{\sqrt{2m_e R^2 kT_e}}. \tag{9}$$

Since we have $J_R^*(E) \le J_R(E)$ from the definition in (7), current would be maximum under the condition $J_R^*(E) = J_R(E)$ for $0 < E < \infty$ [no potential barrier for radius R at least, the second term in the bracket of (8) now reducing to a function of local r and Φ]. This is the orbital-motion-limited (OML) regime; setting $J_R^*(E) \equiv J_R(E)$ in (9) one would find

$$\frac{I_{OML}}{I_{th}} = \left[\sqrt{\frac{4}{\pi}\frac{e\Phi_P}{kT_e}} + \exp\left(\frac{e\Phi_P}{kT_e}\right) erfc\left(\sqrt{\frac{e\Phi_P}{kT_e}}\right)\right] \tag{10}$$

with $erfc$ the complementary error function, and the ratio I_{OML}/I_{th} depending only on $e\Phi_P/kT_e$. At high bias ($e\Phi_P/kT_e$ typically of order 10^3 for tethers) (10) reads

$$\frac{I_{OML}}{I_{th}} \approx \sqrt{\frac{4e\Phi_P}{\pi kT_e}}\left(1 + \frac{kT_e}{2e\Phi_P}\right) \approx \sqrt{\frac{4e\Phi_P}{\pi kT_e}}, \tag{10'}$$

$$I_{OML} \approx 2RLeN_\infty\sqrt{2e\Phi_p / m_e} \qquad (e\Phi_p >> kT_e). \tag{11}$$

For other parameters fixed, the OML current will be reached if R is less than some maximum radius R_{max}. With $E \sim kT_e << e\Phi_p$ we have $J_R(E) \approx J_R(0)$, and Eq.(9) for the general case can be rewritten

$$\frac{I}{I_{OML}} = \int_0^\infty \frac{dE}{kT_e}\exp\left(\frac{-E}{kT_e}\right)\frac{J_R{}^*(E)}{J_R(0)}. \tag{9'}$$

Note that condition $J_r^*(0) = J_r(0)$ suffices to have $J_r^*(E) = J_r(E)$ in the entire range $0 \le E < \infty$ (no potential barrier) for a particular r. From $J_r^2(0) \propto r^2\Phi(r)$ it follows that the no-barrier condition for a radius r is

$$r^2\Phi(r) \le r'^2\Phi(r') \qquad (r \le r' < \infty), \tag{12}$$

Eq.(8) then reading

$$\frac{N_e}{N_\infty} = 1 - \int_0^\infty \frac{dE}{\pi kT_e}\exp\left(\frac{-E}{kT_e}\right) sin^{-1}\frac{J_R{}^*(E)}{J_r(E)}. \tag{13}$$

Also, the OML condition would clearly require the potential to satisfy

$$R^2\Phi_p \le r^2\Phi(r), \qquad (R \le r < \infty). \tag{14}$$

Finally, note that a potential satisfying

$$d(r^2\Phi)/dr \ge 0, \qquad (r_0 \le r < \infty), \tag{15}$$

for some radius r_0, would have no potential barriers in the entire range $r_0 < r < \infty$.

Usually, orbits are analysed by depicting and discussing the family of functions $U_J(r)$ in the energy vs radius plane, with angular momentum as parameter (effective potential formulation [10], [11]); or the family $J_E^2(r)$ in the squared angular-momentum vs radius plane, with energy as parameter (turning-point or impact-parameter formulation [12], [13]). However, conditions (14-15), and the density N_e as a functional of the full potential structure, can be best illustrated by displaying Φ versus Φ_pR^2/r^2, with the ordinate-to-abscissa ratio proportional to $r^2\Phi$ (Fig.1). Condition (15) requires that $\Phi r^2/\Phi_P R^2$ decreases to a minimum when moving away from the origin up to some profile point 0. Figure 1 schematically displays the actual potential profile beyond the OML regime ($I < I_{OML}$); this may be taken as an ansatz that is used in solving Poisson's equation and verified in the solution.

Faraway quasineutrality, $N_e \approx N_i$, shows a behavior $\Phi \sim 1/r$. As one moves up on the profile, $r^2\Phi(r)$ decreases to its minimum at radius r_0. The quasineutral solution remains valid further above, up to a point 1 where $-d\Phi/dr$ diverges; r_1 is a sheath radius. Points 0-1 if drawn to scale would lie very close to the origin in Fig.1 because $e\Phi_0$ and $e\Phi_1$ are of order of kT_i whereas $e\Phi_p/kT_i$ is very large. In the broad region between radii r_1 and R the ion density is negligible, and $r^2\Phi(r)$ reaches a large maximum before dropping to $R^2\Phi_P$ at the probe.

The structure of the r-family of straight lines, $J^2 = J_r^2(E)$ [or $E = U_r(J^2)$] in the J^2-E plane (Fig.2), as considered by Laframboise [11], determines the functions $J_r^*(E)$ and $J_R^*(E)$: Figure 1 serves to illustrate that structure. As r decreases moving up in the potential profile, the line slope steepens monotonically while the line foot $J_r^2(E = 0)$ varies as $r^2\Phi(r)$, the line moving to the left in Fig.2 for all positive energies [and Eq. (13) holding] throughout the range $r > r_0$. Past point 0, however, the line foot moves back to the right till a point m [where $r^2\Phi(r)$ is maximum in Fig. 1] is reached. Since we have $r_m^2\Phi_m > r_1^2\Phi_1 > r_0^2\Phi_0$ and $r_m < r_1 < r_0$, the r-lines in this range generate an envelope in Fig. 2, and result in effective-potential barriers.

The envelope $J^2 = J_{env}^2(E)$ is determined by the equations $J^2 - J_r^2(E) = 0$, $\partial[J^2 - J_r^2(E)]/\partial r = 0$, yielding the parametric representation

$$J^2 = J_{env}^2(r) \equiv -m_e r^3 e\, d\Phi/dr, \tag{16a}$$

$$E = E_{env}(r) \equiv -e\Phi(r) - \tfrac{1}{2} re\, d\Phi/dr. \tag{16b}$$

The envelope touches each line at the point given by Eqs.(16a, b). As the Fig. 1 profile itself, the envelope in Fig. 2 is leftward-concave from the r_0-line to the line for the point of maximum slope in Fig. 1, where it has a cusp, and rightward-concave from there to the m-line. The envelope lies to the ~~left~~ of all lines (making for potential barriers) up to the cusp; right
since it leaves the r_0-line at $E = 0$, and reaches the r_1-line asymptotically as E_{env} and J_{env}^2 (formally) diverge with $-d\Phi/dr$ as $r \to r_1$ in the quasineutral solution, only the range $r_0 - r_1$ counts, in practice, for determining the barriers (Fig.2). [Note that the quasineutral solutions above and below point 0 meet at an angle: condition $E_{env}(r) = 0$ in (16b) corresponds to a minimum of $r^2\Phi$, but the quasineutral solution approaching point 0 from below will have no such property. The full Poisson equation, however, suffices to locally round the profile, with no effect beyond some immediate neighborhood.]

For each radius between r_0 and r_1 only that part of the envelope below the touching point enters in the determination of $J_r^*(E)$; we would thus have

$$J_r^*(E) = J_{env}(E) \;\; [= J_r(E)] \qquad \text{for } E < E_{env}(r) \;\; [> E_{env}(r)]. \tag{17}$$

As r approaches r_1, however, $E_{env}(r)$ diverges, and $J_r^*(E) = J_{env}(E)$ becomes valid for all energies. As Φ rises rapidly with decreasing r above point 1 in Fig.1, the line foot in Fig.2 moves far to the right, the line itself steepening moderately. Within thin layers and broad region we would then have

$$J_r^*(E) = J_{env}(E) \qquad \text{for } E \geq 0 \qquad (r \leq r_1). \tag{18}$$

At the point m of maximum $r^2\Phi(r)$ in Fig.1, the line foot turns again to the left, finally ending at the R-line (Fig.2), which is near-vertical ($E \sim kT_e << e\Phi_P$, $R \ll r_1$). For the conditions of Fig.1, with point 0 lying below the diagonal [condition (14) <u>not</u> satisfied], the R-line lies to the right of the envelope foot. Clearly, Eq.(18) fails in some neighborhood of the probe. At R in particular we have

$$J_R^*(E) = J_{env}(E) \qquad \text{for} \qquad 0 < E < E_c, \tag{19a}$$

$$J_R^*(E) = J_R(E) \approx J_R(0) \qquad \text{for} \qquad E > E_c, \tag{19b}$$

with E_c the energy at the crossing of envelope and R-line. This results in a ratio $I/I_{OML} < 1$. Maximum (OML) current in (9) or (9') would require point 0 to lie at or above the diagonal in Fig.1, the entire R line then appearing to the left of the envelope in Fig.2; with $E << e\Phi_P$ we would have $J_R(E) \approx J_R(0)$, (9') then recovering Eq.(11) for the high-bias OML law.

With $J_R^*(E)$ given by Eqs.(19a, b), and $J_R(E) = J_R(0) = \sqrt{2m_e R^2 e\Phi_P}$, the integral in (9') must be split into separate integrals for intervals $0 < E < E_c$ and $E > E_c$. In the first interval one needs $J_{env}(E)$, which involves the structure of the potential in a narrow radial range. Since the envelope is tangent to both r_0 and r_1 lines, a simple but accurate approximation for $J_{em}(E)$ can be readily obtained without actually knowing $\Phi(r)$,

$$J_{env}^2(E) = J_{r_1}^2(E) - \frac{2m_e(r_1^2 e\Phi_1 - r_0^2 e\Phi_0)^2}{r_1^2 e\Phi_1 - r_0^2 e\Phi_0 + (r_0^2 - r_1^2)E}. \tag{20}$$

We still need to solve for the values r_0, Φ_0, r_1, and Φ_1, which are unknown and depend on the entire potential structure.

Equations to determine those four values are as follows: i) The quasineutrality relation $N_e = N_i$ at point 0, with N_i and N_e given by (3) and (13) respectively, and $J_R^*(E)$ taken from (19a, b). ii) Again, the quasineutrality relation at point 1, with N_e given by (8), where $J_r^*(E)$ is given by (18). iii) Since Eq.(18) holds in some neighborhood below point 1, the derivative of the quasineutrality relation with respect to Φ at r_1 (where $dr/d\Phi$ vanishes) gives a third relation. Those three equations, together with the relation defining E_c,

$$J_{em}(E_c) = J_R(E_c) \approx J_R(0), \tag{21}$$

serve to determine $e\Phi_0/kT_i$, $e\Phi_1/kT_i$, $e\Phi_P R^2/kT_i r_1^2$, and r_1/r_0 as functions of T_e/T_i and E_c/kT_e. Equation (9') now gives

$$I/I_{OML} = \textit{a function of } T_e/T_i,\ E_c/KT_e. \tag{22}$$

One can then obtain $e\Phi_0/kT_i$, $e\Phi_1/kT_i$, $e\Phi_P R^2/kT_i r_1^2$, and r_1/r_0 as functions of T_e/T_i and I/I_{OML}.

[Above point 1 in Fig.1 there are two thin non-quasineutral layers that take the solution to values $\Phi_1 << \Phi << \Phi_P$, and to a radius r_2 a bit closer to the probe. Since the quasineutral solution is singular at r_1, the full Poisson equation must be retained in a layer above point 1, with charge densities expanded around point-1 values. At a radius r_2 close to r_1 the potential itself blows up to infinity, requiring a second non-quasineutral thin layer that just allows a smooth match to the solution in the broad region ranging to the probe [14]. Here we shall take $r_2 = r_1$.]

In the region above the thin layers we have $e\Phi >> e\Phi_1 \sim kT_i$, $e\Phi >> E \sim kT_e$ (Fig.1), making N_i/N_∞ exponentially small. Also, r-lines throughout most of this region are steep and lie far to the right in Fig.2, allowing approximations $J_R^*(E) \sim J_{em}(E) = J_r^*(E) << J_r(E) \approx J_r(0)$ in the integral for N_e/N_∞ in (8) to yield

$$\frac{N_e}{N_\infty} \approx \frac{\kappa}{\pi}\frac{R}{r}\sqrt{\frac{\Phi_P}{\Phi}}, \tag{23}$$

$$\kappa \equiv \int_0^\infty \frac{dE}{kT_e}\exp\left(\frac{-E}{kT_e}\right)\left[2\frac{J_{env}(E)}{J_R(0)} - \frac{J_R^*(E)}{J_R(0)}\right], \tag{24}$$

with κ again a function of T_e/T_i and I/I_{OML}. Note that use of $J_r(E) \approx J_r(0)$ and (18) fails near r_1 and R respectively, and will overestimate N_e, whereas taking $J_R{}^*/J_r$ and J_{em}/J_r small to equate *arc* to *sine* in (8) underestimates N_e and fails near both r_1 and R. Clearly, the error will be smaller the greater the bias.

Introducing new variables,

$$u \equiv \ln\frac{r_1}{r}, \qquad g \equiv \left[\frac{\pi}{\kappa}\frac{\lambda_{Di}{}^2}{R r_1}\sqrt{\frac{kT_i}{e\Phi_P}}\right]^{2/3}\frac{e\Phi}{kT_i}, \tag{25a, b}$$

Poisson's equation, and the boundary conditions imposed by matching to the second layer, become

$$\frac{d^2 g}{du^2} = \frac{e^{-u}}{\sqrt{g}}, \qquad \left[g = \frac{dg}{du} = 0 \quad at \quad u = 0 \quad (g \propto u^{4/3})\right]. \tag{26}$$

This fully determines $g(u)$, which is a parameter-free function. The boundary condition $\Phi = \Phi_P$ at $r = R$ then yields

$$g\left[\ln\frac{r_1}{R}\right] = \left(\frac{\pi}{\kappa}\frac{\lambda_{Di}{}^2}{R r_1}\frac{e\Phi_P}{kT_i}\right)^{2/3}. \tag{27}$$

With both κ and $\sqrt{kT_i/e\Phi_p}\, r_1/R$ functions of T_e/T_i and I/I_{OML}, Eq.(27) yields I/I_{OML} as a function $G(R/\lambda_{De}, e\Phi_P/kT_e, T_e/T_i)$.

Since r_1/R is large, one might use the asymptotic form of $g(u)$ at large u

$$g \approx C\,(u - B), \qquad [C \approx 2.0854, \qquad B \approx 0.3511],$$

near the probe. This potential behavior shows how the high bias makes space-charge effects negligible within some probe neighborhood, $\Phi(r)$ taking the form of a (logarithmic) solution to the 2D Laplace-equation,

$$\Phi \approx \Phi_P\left[1 - \frac{\ln(r/R)}{\ln(r_1/R) - B}\right]. \tag{28}$$

This Laplace behavior will later allow extending results for a wire to probes with arbitrary cross-sections.

The ratio I/I_{OML} is found to be weakly dependent on bias, if high. Also, the dependence on R/λ_{De} and T_e/T_i can be reasonably approximated by a simple law that should be useful in tether design,

$$\frac{I}{I_{OML}} = G\left(\frac{R}{\lambda_{De}}, \frac{e\Phi_P}{kT_e}, \frac{T_e}{T_i}\right) \approx G\left(\frac{R - R_{max}}{\lambda_{De}}\right) = G\left(\frac{R}{\lambda_{De}} - \tilde{R}_{max}\left(\frac{T_e}{T_i}\right)\right). \tag{29}$$

Here $\tilde{R}_{max} \equiv R_{max}/\lambda_{De}$ is roughly a decreasing function of the ratio T_e/T_i, and G is some universal function [$G(0) = 1$, G decreasing with increasing positive argument]. Writing this argument as $(R/R_{max} - 1) \times \tilde{R}_{max}$, one verifies that I/I_{OML} drops faster with R/R_{max} the higher $\tilde{R}_{max}$, i.e. the lower T_e/T_i. At conditions of interest for tethers ($T_i/T_e \sim 1$, $e\Phi_P/kT_e \sim 10^3$) one finds $\tilde{R}_{max} \sim 1$.

The $R = R_{max}$ limit corresponds to $E_c = 0$, with $J_{env}(0) = J_R(0)$ and point 0 lying on the diagonal of Fig.1, giving $I = I_{OML}$. Consider now the OML regime, $R/R_{max} \leq 1$, with $I = I_{OML}$ throughout this radius range. For the non-OML conditions considered until now, the potential profile below point 0 in Fig.1 [determined by using (13) in the quasineutrality equation] varied with $J_R{}^*(E)$, and thus with R/R_{max}. In the OML regime, however, we have $J_R{}^*(E) = J_R(E)$, and thus identical profile, throughout. As R/R_{max} decreases from unity, point 0 just moves down on that particular profile away from the diagonal, with $R^2\Phi_P/r_0{}^2\Phi_0$ decreasing too.

2.2 - ARBITRARY CROSS-SECTION TETHERS

2.2.1 - *Convex cross sections*

The OML current law for a cylindrical probe is very robust. Laframboise and Parker showed that it is valid independently of cross-section shape if convex enough [15], currents to two probes being equal at equal bias, length and cross-section perimeter p. The high-bias current [Eq. (11)] should be written as

$$I_{OML} = \frac{p}{\pi} LeN_\infty \sqrt{\frac{2e\Phi_P}{m_e}} \qquad (e\Phi_P >> kT_e). \qquad (11')$$

Also, OML current density is uniform over the probe surface independently of its shape. The OML law requires that the unperturbed electron distribution function be isotropic but it does not require a rotationally symmetric potential. It holds independently of the ion distribution function, and in the high-bias case it holds independently of the particular isotropic electron distribution. Note, finally, that the ratio I_{OML}/I_{th} is independent of R/λ_{De} and T_e/T_i values over a large domain of validity in the 3D space of parameters R/λ_{De}, T_e/T_i and $e\Phi_P/kT_e$.

For an arbitrary convex cross-section, it remains to determine the domain of OML validity and the current law beyond. For wires the current I was written as [Eq.(29)]

$$I = I_{OML}(p) \times G\left[\frac{R}{\lambda_{De}}, \frac{e\Phi_P}{kT_e}, \frac{T_i}{T_e}\right], \qquad (30)$$

with $I_{OML}(p)$ given by (11') and $G = 1$ for $R = p/2\pi < R_{max} = \lambda_{De} \times \widetilde{R}_{max}(e\Phi_P/kT_e, T_i/T_e)$. We will now show that for any convex cross-section there is some equivalent radius $R_{eq} \propto p$ to be used in (30) the way $R = p/2\pi$ is used for the circle cross-section of a wire.

We first recall that when R is taken larger than R_{max} (or when λ_{De}, and thus R_{max}, decreases with growing density N_∞ at fixed R), the current to a wire drops below the OML value as a size effect related to behavior of the potential profile $\Phi(r)$ far from the probe. For $R \sim R_{max}$ the profile at high bias exhibits a relative minimum of $r^2\Phi(r)$ at certain faraway radius,

$$r_0 \sim R\sqrt{e\Phi_P/kT_e} >> R; \qquad (31)$$

for $R > R_{max}$, that minimum of $r^2\Phi(r)$ lies below its value $R^2\Phi_P$ at the probe. Then, trajectories that hit the probe within some range of glancing angles are unpopulated: the probe being attractive, they come, not from the background plasma, but from other points on the (non-emissive) probe, after having turned back at potential barriers, at large distances $\sim r_0$.

A second important result was that, because of the very high bias (and even though $R \sim \lambda_D$), the space charge has negligible effects within some extended region around the probe, where the Laplace equation holds and the potential $\Phi(r)$ takes the form [Eq. (28)]

$$\Phi/\Phi_P \approx 1 - \alpha \ln(r/R), \qquad R \leq r << r_0 \tag{32}$$

$$1/\alpha \sim \ln(r_0/R) \sim \ln\sqrt{e\Phi_P/kT_e} \qquad \text{(moderately large).} \tag{33}$$

The fact that the potential obeys the Laplace equation over a large probe neighborhood proves now essential in allowing to extend the analysis of wires to probes with arbitrary cross section by determining the proper radius R_{eq}.

Elliptical cross sections may be directly analysed by using elliptical coordinates v, w, describing a family of confocal ellipses and hyperbolas. With x, y cartesian coordinates in the cross-section plane, and $w(x, y) = const$ representing the ellipses, which rapidly approach circles as w increases, any value $w = w_P$ serves to describe an elliptical cross-section. Because of the high bias, the Laplace equation is again valid within an extended probe vicinity, which reaches where w ellipses are near-circles,

$$w \approx \ln(2r/a) \qquad \text{for} \qquad w > w^* \qquad (w^* = 1.5, \text{ say}), \tag{34}$$

where $2a$ is distance between foci. It may be shown that $\Phi(v, w)$ is nearly independent of v everywhere, although the electric field will be nearly radial for $w > w^*$ only [7]. The simplified Laplace equation for the probe vicinity then yields

$$d^2\Phi/dw^2 \approx 0 \quad \Rightarrow \quad \Phi/\Phi_P \approx 1 - \alpha(w - w_P). \tag{35}$$

Within some limited w-range beyond w^* we have, using (34),

$$\Phi/\Phi_P \approx 1 - \alpha \ln(r/R_{eq}), \tag{36}$$

Beyond w^*, the potential behaves as in the case of a circle of radius R_{eq}, the coefficient α being taken from the solution for a circle of that radius. For ellipses of eccentricity ~~0 and 1~~, corresponding to thin tapes $(w_P = 0)$ and circles, one finds $R_{eq} = p/8$ and $R_{eq} = p/2\pi$ respectively.

Equation (36) for the elliptical cross section may be rewritten as

$$\frac{\Phi}{\Phi_P} = \frac{-\ln(r/r_\infty)}{\ln(r_\infty/R_{eq})} = -\alpha \ln\frac{r}{r_\infty}, \tag{37}$$

where the radius r_∞ was defined by writing $\ln(r_\infty/R_{eq}) \equiv 1/\alpha$, thus being comparable to r_0. To determine R_{eq} for a general case, one solves the Laplace equation between the contour of the given cross section, where $\Phi = \Phi_P$, and a circle of radius $r_\infty >> p$, where Φ vanishes; far from the cross section the potential will take the form of Eq.(37). This classical problem, of interest for transmission lines, relates to the determination of the capacity per unit length C_l between two cylinders; with the electric field nearly radial at the outer circle one readily finds, using (37), $C_l \approx 2\pi\varepsilon_0\alpha = 2\pi\varepsilon_0/\ln(r_\infty/R_{eq})$.

Conformal mapping, expansions in circular harmonics, and image methods have been used to determine C_l in electrostatics, and thus R_{eq} here, for a variety of cross sections. As examples, for a square, an equilateral triangle and a right-angle isosceles triangle one finds $R_{eq} \approx p/6.78$, $R_{eq} \approx p/7.11$, and $R_{eq} \approx p/8.28$, respectively. One can thus determine the equivalent radius $R_{eq} \propto p$ for a general convex cross section characterised by its perimeter p. The OML law will keep valid as regards size as long as R_{eq} remains below R_{max}, current beyond being given by (30) with R_{eq} replacing R. Shape details are irrelevant to the size effect; the Laplace equation, valid near the probe, filters out to the far field all information on shape except for the equivalent radius R_{eq}.

2.2.2 - *Non-convex cross sections*

The OML law will again fail for a non-convex cross section if too large. In addition, however, the law now also fails as a shape-effect independent of size. Either type of failure relates to a quite different feature in the potential field. OML failure due to shape relates to the behavior of the potential field <u>near</u> the probe, ultimately dependent on the degree of cross-section convexity. For a thin tape, for instance, one finds

$$I/I_{OML}(p) \approx 1 - \gamma\alpha^2 \qquad \text{for} \qquad R_{eq}\ (= p/8) < R_{max}. \qquad (38)$$

The current reduction described by (38) can be understood by noticing that, for any point on the tape, trajectories that would hit it within some (very narrow) range of glancing angles are unpopulated: they would had come from other points on the tape, having kept close to it throughout. This current reduction holds no matter how small R_{eq} or p. On the other hand, shape is here determinant. Equation (38) holds for any elliptical cross section with coefficient γ depending on eccentricity; for a cross section evolving from thin tape to circle, γ will finally vanish at certain eccentricity, the OML current law holding in the limit case of a $(R < R_{max})$ circle.

For repelled particles, all trajectories leaving (backward in time) from a point in a non-concave probe reach back to infinity; this leads to the old result that current to a *retarding* probe is independent of probe shape. Attracted particles, however, might actually return to a probe not convex enough. Such a trajectory must become tangent from the inside to some equipotential line of lower curvature at the turning point [15]. This can only hold in a thin layer next to the tape. To determine how potential barriers in this layer reduce the current, it suffices to consider trajectories in the near potential field, $\Phi = \Phi_P\,[1 - \alpha w(x, y)]$, leaving points in the tape at small upward glancing angles to either right or left. The calculations give $\gamma \approx 0.058$. Although a tape thus comes out not to be convex enough, its shape failure is quite weak; with α [given by (33)] logarithmically small for the bias of interest, the current in (38) lies less than 1% below the OML value.

The reduction of current below the OML value for cross sections that are small can be substantial if they present definitely concave segments. Trajectories that hit a point on a concave segment would be unpopulated over a wide range of incoming angles. The OML law, nonetheless, may still be used to great accuracy if the actual full perimeter p is replaced in (30) by the perimeter p_{eq} of the minimum-perimeter (convex) envelope of the cross section, made of segments of the actual cross section and of straight connecting segments. For a cross section made of two adjoining circles, for instance, we would have $p_{eq} \approx 0.82p = 6.55\,R_{eq}$, with R_{eq} taken from exact results for the capacity per unit length between the two-circle cylinder and a large, centered, circular cylinder.

To understand why Eq.(30) holds when p is replaced by p_{eq} note that *i*) the value of $\sqrt{\Phi(r)}$ averaged over the minimum-perimeter envelope may be shown to be extremely close to the value $\sqrt{\Phi_P}$ in (30); *ii*) all trajectories reaching the envelope from the faraway plasma would certainly hit the probe; and *iii*) conditions in the vicinity of the *straight* connecting segments would be similar to conditions around a tape as far as convexity is concerned, resulting in current reduction that is fully negligible as in Eq.(38). Note that point *ii*) would fail for any convex envelope of larger perimeter, while point *iii*) would fail for a concave envelope lying between the actual cross section and its minimum-perimeter envelope (trajectories reaching such a concave envelope within a sensible range of incoming angles would be unpopulated). Introducing the value p_{eq} allows accurate use of the OML law for non-convex cross sections.

2.2.3 - *Cross sections made of disjoint parts*

Based on issues such as survivality, use of multiline tethers has been suggested. Consider the case of two disjoint circles with centers at moderate distance. Here the mere concept of a minimum-perimeter envelope proves unsatisfactory, p_{eq} exceeding the full perimeter p. This failure relates to condition *ii*) in Sec. 2. 2. 2. For non-adjoining probes such as these, not all trajectories arriving from the faraway plasma at the straight segments connecting the circles would hit the probe; some trajectories reach opposite connecting segments and escape.

Although the current density at those connecting segments may have the OML value, only some fraction f will correspond to trajectories reaching either circle. The OML law may still be used, however, if p_{eq} is replaced by some effective perimeter p_{eff} accounting for f. This factor is easily determined because trajectories are approximately straight inside the minimum-perimeter envelope, $\sqrt{\Phi(r)}$ averaged over the envelope still being close to the actual value $\sqrt{\Phi_P}$ on the cross sections. This results in a vector velocity that is nearly constant. For a distance between centers four times the radii, say, we readily find $p_{eff} \approx 0.92p$. Note that this simple calculation would fail for distance between centers large, when trajectories between circles could not be approximated as straight; one could still determine f, however, by solving for trajectories in the Laplace near field.

Results for R_{eq}, p_{eq}, and p_{eff} serve to determine collection interference in multiline tethers.

3 - ELECTRON COLLECTION OR EJECTION BY PLASMA CONTACTORS

3.1 - DOUBLE-LAYER CONTACTORS

3.1.1 - *The spherical collector*

Consider again electron collection, as in Sec. 2, but now let the collector, say a Langmuir probe, be spherical. One can readily obtain equations for electron density and current in this 3D geometry, corresponding to Eqs. (8) and (9),

$$\frac{N_e}{N_\infty} = \int_0^\infty \frac{dE}{kT_e} \exp\left[\frac{-E}{kT_e}\right] \frac{J_r(E) + \sqrt{J_r^{2}(E) - J_R^{*2}(E)} - 2\sqrt{J_r^{2}(E) - J_r^{*2}(E)}}{\sqrt{\pi}\,\sqrt{2m_e r^2 kT_e}}, \tag{39}$$

$$\frac{I}{I_{th}} = \int_0^\infty \frac{dE}{kT_e} \exp\left[\frac{-E}{kT_e}\right] \frac{J_R^{*2}(E)}{2m_e R^2 kT_e}. \tag{40}$$

In Eqs. (39) and (40), $I_{th} \equiv 4\pi R^2 eN_\infty \sqrt{kT_e / 2\pi m_e}$ is the random current, and $J_r(E)$ and $J_r^*(E)$ are again defined by Eqs. (6) and (7). The 3D OML current would be obtained by taking $J_R^*(E) = J_R(E)$, $0 < E < \infty$, yielding $I_{OML}/I_{th} = 1 + e\Phi_P/kT_e$. At high bias and for probes of equal area, the 3D OML-current is much greater than the 2D OML-current. As now shown, however, the 3D OML law is never reached.

Quasineutrality here yields a faraway behavior $\Phi \sim 1/r^2$, profile slope thus being finite at the origin of Fig. 1, as opposed to the 2D case. The OML law would now require a profile slope $a > 1$ $[\Phi \approx a \times \Phi_P R^2/r^2]$. Setting $J_R^*(E) \equiv J_R(E)$ in (39) and assuming the profile is downward concave $[J_r^*(E) \equiv J_r(E)]$, and using Eq. (3) for N_i and condition $e\Phi_P/kT_e >> 1$, we find $a \approx 1/[2(1 + T_e/T_i)] < 1$, contrary to the hypothesis. If the profile turned upwards as it leaves the origin, there would exist a line envelope in Fig. 2, with $J_r^*(E) = J_{env}(E)$ for $E < E_{env}(r)$, and $J_r^*(E) = J_r(E)$ for $E > E_{env}(r)$ [see Eq. (17)]. Since $E_{env}(r)$ in Eq. (16b) arises from deviations from $(\Phi \sim 1/r^2)$-behavior of order higher than $1/r^2$, the contribution from the last term in the last fraction in (39) can still be ignored, as with the downward concave profile.

We note that the conclusion that the 3D OML current is never reached is not dependent on a high-bias condition. For $e\Phi_P/kT_e$ small, in particular, one just needs to replace Eq. (3) with the equation [see Ref. 14]

$$\exp\left(\frac{e\Phi}{kT_i}\right)\times\frac{N_i}{N_\infty} = 1-\frac{1}{2g(0)}\left[g(\lambda)-\sqrt{1-\frac{R^2}{r^2}}\,g\left(\frac{\lambda}{1-R^2/r^2}\right)\exp\left(\frac{\lambda R^2/r^2}{1-R^2/r^2}\right)\right], \tag{41}$$

$$g(\lambda) \equiv \int_\lambda^\infty \sqrt{\xi}\,e^{-\xi}\,d\xi, \qquad \lambda \equiv \frac{e(\Phi_P-\Phi)}{kT_i}. \tag{42}$$

Assuming a profile slope at the origin in Fig. 2, $a > 1$, we find $a = 1/2 < 1$.

With $a < 1$ the profile must turn upwards as it leaves the origin; hence, there always exists a line envelope in Fig. 2, with $J_R^*(E) < J_R(E)$ over some energy range. At high bias the slope at the origin is then

$$2(1+T_e/T_i)a \approx \int_0^\infty \frac{dE}{kT_e}\frac{\exp(-E/kT_e)}{\sqrt{\pi E/kT_e}}\frac{J_R^{*2}(E)}{2m_eR^2 e\Phi_P} \sim \frac{I}{I_{OML}}. \tag{43}$$

If $e\Phi_P/kT_e$ is large but λ_{De}/R is small, the ratio I/I_{OML}, and thus the slope a, is small [with $J_R^*(E) << J_R(E)$ over a substantial E-range in Eqs. (40) and (43)]. An approximate analysis shows the plasma to be quasineutral beyond a sheath radius r_{sh} such that

$$I/I_{th} \sim r_{sh}^2/R^2, \tag{44}$$

with a sheath equation (setting $T_i = T_e \equiv T_\infty$ to ignore any T_i/T_e dependency)

$$\frac{(\lambda_{D\infty}/R)^{4/3}e\Phi_P/kT_\infty}{(I/I_{th})^{2/3}} \approx F_P\left(\frac{r_{sh}}{R}\right). \tag{45}$$

For $(\lambda_{D\infty}/R)^{4/3}e\Phi_P/kT_\infty$ small, the function F_P is small, with $r_{sh}/R \approx 1$ and $I/I_{th} \approx 1$. The slope a decreases fast with increasing bias $(a \sim kT_e/e\Phi_P)$ and the profile in Fig. 1 follows a thin sheath behavior: it keeps low for almost the entire radial range, suddenly rising to the value $\Phi = \Phi_P$ at the probe. For $(\lambda_{D\infty}/R)^{4/3}e\Phi_P/kT_\infty$ large, the profile rises above the diagonal near the origin (thick sheath, $r_{sh} >> R$), but a keeps decreasing, though slowly, with increasing bias, $a \sim (kT_e/e\Phi_P)^{1/7} \times (\lambda_{De}/R)^{8/7}$. There is now a probe neighborhood where space-charge has negligible effects and the potential follows a 3D Laplace behavior, $\Phi/\Phi_P \approx R/r$ (the slope profile at the right top corner in Fig. 1 being ½). F_P is now linear in r_{sh}/R, leading to [14]

$$(\lambda_{D\infty}/R)^{4/3}e\Phi_P/kT_\infty \sim (I/I_{th})^{7/6}. \tag{46}$$

3.1.2 - *Core/double-layer contactor regime*

At fixed bias Φ_P and radius R, the electron current collected (now called $I_{e,an}$) can be increased by using an "active" collector or plasma contactor (a Hollow Cathode working as anode), which expels an ion current $I_{i,an}$ while producing a plasma in its neighborhood; subscript *an* refers to current $I_{e,an}$ being collected (anodic) and current $I_{i,an}$ being ejected. In keeping the geometrical symmetry of the previous analysis for just discussing contactors, we assume that some representative radius R can be assigned to the contactor and that the flow follows a spherical sector geometry; at the end all currents should be scaled down by the ratio between its solid angle and 4π. As $I_{i,an}$ is increased from zero, a thick sheath gets thicker while its net negative charge decreases, until a critical ion current is reached for which the net charge vanishes and the sheath becomes a double layer. At ion currents above critical, the double layer lies detached from the contactor, sandwiched between the quasineutral region beyond r_{sh} and a quasineutral core in the range $R < r < r_{DL}$ (inner radius of the double layer).

An approximate but comprehensive analysis of plasma contactors solves separately for the three regions above in a simplified way [16]. Only the ambient particles, both collected (electrons) and rejected (ions) enter the solution for the region beyond r_{sh}, which recovers Eq. (44),

$$I_{e,an} / I_{e,th} \sim r_{sh}^2 / R^2. \tag{44'}$$

The double-layer structure is determined by the collected and ejected species (ambient electrons, contactor ions), yielding

$$\frac{(\lambda_{D\infty} / R)^{4/3} e\Phi_P / kT_\infty}{(I_{e,an} / I_{e,th})^{2/3}} \quad \textit{as function of} \quad \frac{r_{DL}}{r_{sh}}, \ \frac{I_{e,an}\sqrt{m_e}}{I_{i,an}\sqrt{m_{ic}}}, \tag{47}$$

$$\frac{\Phi(r_{DL})}{\Phi_P} \quad \textit{as function of} \quad \frac{r_{DL}}{r_{sh}}, \ \frac{I_{e,an}\sqrt{m_e}}{I_{i,an}\sqrt{m_{ic}}}. \tag{48}$$

Only the plasma species produced by the contactor, both ejected (ions) and confined (electrons) enter the solution for the core, yielding

$$\frac{R}{r_{DL}} \quad \textit{as function of} \quad \frac{e\Phi_P}{kT_{ec}}\left[1 - \frac{\Phi(r_{DL})}{\Phi_P}\right]. \tag{49}$$

Equations (44') and (47)-(49) determine

$$\frac{I_{e,an}}{I_{e,th}} \quad \textit{as function of} \quad \left(\frac{\lambda_{D\infty}}{R}\right)^{4/3} \frac{e\Phi_P}{kT_\infty}, \ \frac{e\Phi_P}{kT_{ec}}, \ \frac{I_{i,an}\sqrt{m_{ic}}}{4\pi R^2 e N_\infty \sqrt{kT_\infty / 2\pi}}. \tag{50}$$

Here m_{ic} and T_{ec} are contactor ion mass and electron temperature.

At the critical ion current, Eq. (49) is an identity $[\Phi(r_{DL}) = \Phi_P$ at $r_{DL} = R]$ and (48) gives a relation

$$\frac{I_{e,an}\sqrt{m_e}}{I_{i,an}\sqrt{m_{ic}}} = \alpha_{WW}\left(\frac{R}{r_{sh}}\right), \qquad at\ critical. \tag{51}$$

Equation (51) is the so-called Langmuir relation for the structure of a double layer with particles that enter it from both sides having kinetic energies small against the potential energy jump, $e\Phi_P$. Wei and Wilbur gave $\alpha_{WW} \sim 1/8$ at R/r_{sh} small, and $\alpha_{WW} = 1$ at $R/r_{sh} \approx 1$ (planar double layer) [17]. Usually the double layer gets thinner as $I_{i,an}$ is increased beyond its critical value.

A plasma contactor serves to reach higher values of the current ratio $I_{e,an}/I_{e,OML}$, which otherwise would be very small at the high bias and low $\lambda_{D\infty}/R$ of interest. The $I_{e,an}/I_{e,OML}$ ratio clearly has unity as upper bound. This makes for an upper bound on the ion current emitted itself; actually, such bound would overestimate the maximum ion current that can be ejected, because the electron current will again not attain its OML value. Setting $T_i = T_e$ and adding $N_i\ (emitted) \approx I_{i,an}/4\pi r^2 e\sqrt{2e\Phi_P/m_{ic}}$ to the quasineutrality condition, $N_i + N_i\ (emitted) \approx N_e$, at faraway distances, Eq. (43) reads

$$a \approx \frac{I_{e,an}}{I_{e,OML}}\left[\frac{1}{4}+\frac{1}{4\sqrt{\pi}}\frac{I_{i,an}\sqrt{m_{ic}}}{I_{e,an}\sqrt{m_e}}\times\sqrt{\frac{kT_\infty}{e\Phi_P}}\right].$$

The ratio $I_{i,an}\sqrt{m_{ic}}\ /\ I_{e,an}\sqrt{m_e}$, which had a maximum about 8 at critical, decreases above critical [see Fig. 2 in Ref. (16)]. Since $e\Phi_P/kT_e$ is large, we necessarily have $a < 1$ and thus $I_{e,an} < I_{e,OML}$.

Plasma contactors may also eject electrons (Field-emission Arrays are being considered at present as alternative active cathodes). Operation of cathodic and anodic plasma contactors exhibits certain symmetry in case of equal ion and electron contactor temperatures. With $I/I_{th} \propto I\sqrt{m}$, the general Eq. (1) for passive collection, which is valid for cylinders and spheres, shows that the electron and ion currents to corresponding collectors (equal radius and opposite bias), satisfy the symmetry relation, $I_{i,cat}\sqrt{m_{ia}} = I_{e,an}\sqrt{m_e}$. Here m_{ia} is the ambient ion mass and subscript *cat* labels current $I_{i,cat}$ as collected (cathodic); for temperatures unequal but comparable, as in the ionosphere, the discussion that follows would suffer no basic modification. The symmetry above can also be seen in the detailed equations (44) and (45). In case of active collection, and assuming $T_{ic} = T_{ec}$, the respective detailed equations (44') and (47)-(49) show that equal values of $I_{e,cat}\sqrt{m_e}$ and $I_{i,an}\sqrt{m_{ic}}$ for corresponding contactors, lead to equal values of $I_{i,cat}\sqrt{m_{ia}}$ and $I_{e,an}\sqrt{m_e}$. Note that ambient-to-contactor ion mass ratio $m_{ic}/m_{ia} \neq 1$ and (common ion, electron) temperature ratio $T_c/T_\infty \neq 1$ do not break the symmetry.

In spite (or because) of this symmetry, an active collector has effects dramatically different for anodic and cathodic contact. This is because the disparity of masses makes the electron current (whether collected or emitted) dominant. In the anodic case, the contactor just makes the collected electron current closer to its upper bound $I_{e,OML}$, as mentioned. In the cathodic case, it both makes the collected ion current closer to its own upper bound $I_{i,OML}$ [even if negligibly ($\sqrt{m_e/m_{ia}}$-times) smaller than $I_{e,OML}$] and allows for an ejected electron current about $\sqrt{m_i/m_e}$-times greater.

3.2 - CATHODIC CONTACTOR VERSUS ANODIC CONTACTOR

Clearly, passive ion collection is highly inefficient, making active contact necessary for cathodic charge-exchange. The question remains whether anodic and cathodic contactors can attain comparable currents. There is general consensus that cathodic contact is easier or more effective. We now show in this respect that the symmetry of Eqs. (44'), (47)-(49), discussed in Sec. 3. 1. 2, is broken by a number of physical effects.

Actually, cathodic contact is favored, in a sense, by that symmetric system itself, a fact again arising from the electron current (whether collected or emitted) being dominant. Consider an anodic contactor at critical ($r_{DL} = R$). Using (51) in (47) with $r_{DL} = R$ one finds

$$\frac{(\lambda_{D\infty}/R)^{4/3} e\Phi_P / kT_\infty}{(I_{e,an}\sqrt{m_e})^{2/3}} \quad as\ function\ of \quad \frac{r_{sh}}{R},$$

and, using (44'),

$$I_{e.an}\sqrt{m_e} \quad as\ function\ of \quad (\lambda_{D\infty}/R)^{4/3} e\Phi_P / kT_\infty .$$

Clearly, $I_{i,cat}\sqrt{m_{ia}}$ will have the same value for the corresponding cathodic contactor at critical itself. Since the ratio r_{sh}/R will then be equal for both contactors, Eq. (51) shows that the emitted currents will satisfy $I_{e,cat}\sqrt{m_e} = I_{i,an}\sqrt{m_{ic}}$. Equation (51), again, yields

$$\frac{I_{e,an}}{I_{e,cat}} = \alpha_{WW}\left(\frac{R}{r_{sh}}\right).$$

Note that current to the cathodic contactor can be as high as 8 times the current to the corresponding anodic contactor, both at critical. A similar result is found beyond critical, when comparing contactors collecting currents that are equal fractions of the respective OML currents, $I_{e,an}/I_{e,OML} = I_{i,cat}/I_{i,OML}$.

The ambient plasma is a first source of asymmetries, arising from B_0 and U_{sat} effects. We first argue that such effects, which were ignored in Sec.2, are indeed negligible for bare-tether electron collection. As regards the geomagnetic field B_0, there exists an upper bound to the current to a probe in a magnetised collisionless plasma, the Parker-Murphy law. At high bias, in 2D geometry, one has

$$I_{PM} \approx I_{OML}\sqrt{\frac{\pi}{2}\frac{l_{e0}}{R}}.$$

This suggests that if R is much less than l_{e0} (ambient electron gyroradius), the I_{PM} bound then lying well above I_{OML}, the OML current should hardly be affected by magnetic effects. Actually, the PM law makes no space-charge consideration. When space-charge is taken into account, a second condition is required for magnetic effects to be negligible, namely $\lambda_{De} << l_{e0}$ [7]. Taking $R \sim \lambda_{De}$, both conditions are reasonably satisfied by a tether in LEO orbit.

Regarding U_{sat} effects in 2D geometry, we note that, as discussed in Sec. 2. 2, the 2D OML law does not require rotational symmetry. However, the mesothermal character of the flow [U_{sat} small (large) compared with electron (ion) thermal velocity] results in a paradox. The faraway electron population would still be (nearly) isotropic; Laframboise and

Parker showed that N_e is then necessarily less than N_∞ [15]. On the other hand, the hypersonic ion flow will result in N_i exceeding N_∞ in a broad region on the ram side of the flow. Quasineutrality would thus be violated in a region of dimension much larger than λ_{De}. The resolution of the paradox seems to lie on $E < 0$ electrons trapped in bound trajectories not accounted for by Laframboise and Parker. The collisional trapping rate proves too slow [7], the key process being collisionless (adiabatic) trapping [18], [19]. As troughs in electron potential energy develop when quasineutrality is originally broken, electrons are trapped in a process that is adiabatic (in the mechanical sense) because the ion motion controlling Φ time-variations is slow compared with the motion of electrons in their bound orbits.

The 3D case is quite different as manifest in the TSS1R-tether results [20]. Current not being OML, U_{sat} effects on the flow are determinant for collection; also, R was there much greater than l_{e0} (and λ_{De}). Both effects hold for a contactor, its smaller "radius" still being greater than both λ_{De} and l_{e0}. Geomagnetic field effects affect electrons and definitely favor cathodes because the gyroradius of electrons they eject is greater than l_{e0} and increases as their flow diverges outwards. Spacecraft velocity effects affect ions. Whatever their character, they should be weaker for a cathode, which will collect ions from all directions under a (negative) bias that is typically several times the ion ram energy (~ 5 eV).

The core is also a source of asymmetries, though no definite consequences are clear. First, note that electrons accelerated by the double layer into the core of an anodic contactor may result in ionization external to the contactor, helping to drive the ion current that sustains the double layer itself. There is no such effect in case of a cathode, which accelerates electrons out to the ambient quasineutral region. While often relevant in the laboratory, external ionization will probably make no effect, however, at the lower neutral densities found in orbit.

Secondly, our assuming equal temperatures $T_{ic} = T_{ec}$ in Sec. 3. 1. 2 will not hold in general. In the plasma produced by the contactor, whichever species are ejected and confined, ions will have temperatures comparable to ambient ion and electron temperatures (~ 0.1 eV), whereas electrons are typically one order of magnitude hotter (~ 1 eV). This breaks the symmetry between cathodic and anodic operations, although effects are somewhat balanced. Consider again corresponding contactors at collected currents that are equal fractions of the respective OML current, $I_{e,an}/I_{e,OML} = I_{i,cat}/I_{i,OML}$. As can be seen in Fig. 2 of Ref. 16, the anode will now require a comparatively greater emitted current. On the other hand, the ratio $I_{e,an}/I_{e,cat}$ is also increased.

Although a full, satisfactory model of contactors is lacking, there is, finally, a clear basic asymmetry between cathodes and anodes in the physics of the contactor itself. Electrons are produced inside the contactor by both thermoionic emission and ionization of flowing (usually xenon) atoms. Ions, which are required to sustain quasineutrality inside, are only produced by ionization. In the case of an anode, the steady supply of xenon is directly related to the ion current ejected; electrons cannot escape, and are continuously returning to the contactor. In the case of a cathode, however, there is no such direct relation between xenon supply and the core, double-layer, and ambient regions outside. Ions return to the contactor continuously and escape indirectly by leaving as neutrals.

4 - CHARGE BALANCE IN THE ISS

Use of bare tethers for reboost of the International Space Station, to maintain its approximate circular orbit, was formally proposed to NASA in 1996 [21]. The baseline ISS reboost method is a traditional bi-propellant rocket thruster that must be refueled by Soyuz-Progress vehicles. Substantial savings would result from using tethers instead of chemical thrusting. Operational and technical issues on BT reboost, such as safety concerns on Shuttle rendez-vous and flight path, and the impacts of tether-libration and off-angle thrust on microgravity environment and long-term ISS orbit, are still being discussed [22]. The natural downwards deployment for thrusting might not be the favored option.

Use of bare tethers as secondary power-generation system was proposed to NASA in 1996 too. A NASA (Marshall Space Flight Center) experiment to test bare-tether collection, the Propulsive Small Expendable Deployer System (ProSEDS), is tentatively scheduled to be set in orbit in August 2002 [23]. Preliminary laboratory tests on collection have shown reasonable agreement between theoretical formulations and experimental data [24], [25]. Actually, bare-tether collection has already been verified on board the ISS.

The ISS structure is electrical ground for the station. Because of the ISS high-voltage power-generation system, exposed electrical cell connections on the photovoltaic arrays are 160 V positive relative to ground. Such connections may collect up to 0.4 A from the ionosphere. It has been estimated that in the absence of any mitigation, the Station, if not in eclipse, or its solar-array active side in the wake, could be forced to float as much as 120 V negative to the plasma, to make its entire structure act as a passive ion collector [3], [26]. Most ISS surfaces are anodized with a thin dielectric coating. Arcing might then lead to dielectric breakdown, giving rise to a variety of hazards.

As a control strategy, the ISS carries onboard two Hollow-Cathode, xenon plasma contactors. Each contactor is able to eject up to 10 A at negative bias below 20 V. This will practically "clamp" the ISS strusture to the ionospheric plasma potential for all reasonable conditions. The current emitted by the contactor is measured in real time. A complex instrument on board the ISS (FPP = Floating Potential Probe), which includes a Langmuir probe, was in function since late 2000, to measure ionspheric plasma conditions. A complex computer code, Environment WorkBench (EWB), integrates models for orbital motion, ionosphere, geomagnetic field, and ISS geometry.

In the early months of 2001 the ISS contactor regularly showed night-time currents reaching above 0.1 A. It was realized that the station was then passing repeatedly over the southern auroral oval south of Australia, and its greater associated density; yet, the active side of the arrays were in the wake and the EWB code could not account for the current emitted by the contactor. Also, when contactors were switched off as a test on the ISS, the EWB code again showed disagreements with ISS potentials measured by the FPP.

It was then realized that each solar array mast, 40 m long, has around 400 m of tensioning rods made of stainless steel. At the magnetic latitudes of interest, the geomagnetic field is near vertical; also at the periods considered, the masts were both nearly horizontal and perpendicular to the orbital velocity. This results in maximum motionally induced field in the rods. When the bare-tether collection model under the induced bias was included in the EWB code, near perfect agreement was found between data and code predictions on both current, with contactor on, and floating potential with contactor off [3].

BIBLIOGRAPHY

1. M. Martínez-Sanchez and J.R.Sanmartín, J.Geophys.Res. **102**, 27 254 (1997).
2. J. R. Sanmartin and E. Ahedo, *Permanent Spacecraft-Ionosphere Exchange Currents*, Modelling of S/C-Plasma Interactions/ESTEC-ESA, Noordwijk, 24-25 February 2000.
3. E. A. Bering, S. Koontz, I. Katz, B. Gardner, D. Evans, and D. Ferguson, *The Plasma Environment of the International Space Station in the Austral Summer Auroral Zone Inferred from Plasma Contactor Data*, Paper 2002-0935, 40th AIAA Aerospace Sciences Meeting and Exhibit, Reno, NV, 14-17 January 2002.
4. J. R. Sanmartín, E. Ahedo and M. Martínez-Sanchez, *An Anodeless Tether Generator*, in Physics of Charged Bodies in Space (ed. M. Dobrowolny, Editrice Compositori, Bolonia), 201-208 (1992); J. R. Sanmartín, M. Martínez-Sanchez and E. Ahedo, J. Propul. Power **9**, 353 (1993).
5. R.D.Estes, J.R.Sanmartin, and M. Martinez-Sanchez, J. Spacecraft & Rockets **37**, 197 (2000).
6. J. R. Sanmartín, R. D. Estes and E. Lorenzini, *Efficiencies of Different Types of ED-Tether Thrusters*, in Space Technology and Applications International Forum 2001 (ed. M. S. El-Genk, American Institute of Physics, New York), 479-487 (2001); E. Ahedo and J. R. Sanmartín, J. Spacecraft & Rockets **39**, to appear (2002).
7. J. R. Sanmartín and R. D. Estes, Phys. Plasmas **6**, 395 (1999).
8. R. D. Estes and J. R. Sanmartín, Phys. Plasmas **7**, 320 (2000).
9. J. R. Sanmartín and R. D. Estes, Phys. Plasmas **8**, 4234 (2001).
10. I. B. Berstein and I. N. Rabinowitz, Phys. Fluids **2**, 112 (1959).
11. J. G. Laframboise, *Theory of Spherical and Cylindrical Langmuir Probes in a Collisionless Maxwellian Plasma at Rest*, Univ. Toronto Intitute for Aerospace Studies Report No. 100, June 1966.
12. D. Bohm, E. H. S. Burhop and H. S. W. Massey, *The Use of Probes for Plasma Exploration in Strong Magnetic Fields*, in Characteristics of Electrical Discharges in Magnetic Fields (A.Guthrie and R.K.Wakerling, eds, McGraw-Hill, New York, 1949), Chap. 2.
13. L. W. Parker, *Computer Method for Satellite Plasma Sheath in Steady-State Spherical Symmetry*, US Air Force Report AFCRL-TR-75-0410, July 1975.
14. S. H. Lam, Phys. Fluids **8**, 73 (1965).
15. J.G.Laframboise and L.W.Parker, Phys. Fluids **16**, 629 (1973).
16. E. Ahedo, M. Martinez-Sanchez and J. R. Sanmartin, Phys. Fluids B **4**, 3847 (1992).
17. R. Wei and P. J. Wilbur, J. Appl. Phys. **60**, 2280 (1986).
18. A. V. Gurevich, Soviet Physics JETP **26**, 575 (1968).
19. T. Onishi, M. Martínez-Sánchez, D. Cooke and J. R. Sanmartín, *PIC Computation of Electron Current Collection to a Moving Bare Tether in the Mesothermal Condition*, Paper IEPC-01-245, 27th International Electric Propulsion Conference, Pasadena, CA, 15-19 October, 2001.
20. D. L. Cooke and I. Katz, Geophys. Res. Lett. **25**, 753 (1998).
21. R. D. Estes, E. Lorenzini, J. R. Sanmartín, J. Pelaez, M. Martínez-Sanchez, L. Johnson, and I. Vas, J.Spacecraft & Rockets **37**, 205 (2000).

22. J. H. Blumer, B. B. Donahue and M. E. Bangham, *Practicality of using a Tether for Electrodynamic Reboost of the International Space Station*, in Space Technology and Applications International Forum 2001 (ed. M. S. El-Genk, American Institute of Physics, New York), 445-451 (2001);
23. L. Johnson, R. D. Estes, E. Lorenzini, M. Martínez-Sanchez, and J. R. Sanmartín, J.Spacecraft & Rockets **37**, 173 (2000).
24. B. E. Gilchrist, S. G. Bilen and A. D. Gallimore, *Current Collection to Long, Thin Probes in a Dense High-Speed Flowing Plasma*, in Space Technology and Applications International Forum 2001 (ed. M. S. El-Genk, American Institute of Physics, New York), 494-501 (2001)
25. M. Kruijff, E. J. van der Heide, G. Vannaroni, M. Dobrowolny and F. De Venuto, *Long Term Stability of Bare Conductive Tethers: Combined Results from Plasma Chamber Tests and Advanced Simulations*, Space Technology and Applications International Forum 2001, Albuquerque, NM, 11-14 February, 2001.
26. D. C. Ferguson, G. B. Hillard and T. L. Morton, *The Floating Potential Probe (FPP) for ISS - Operations and Initial Results*, in SP-476 7th Spacecraft Charging Technology Conference (eds. A Hilgers and E.Daly, ESTEC-ESA, Noordwijk), 365-370 (2001).

Figure Captions

1 Schematics of potential Φ versus $\Phi_P R^2/r^2$ for $R > R_{max}$ (maximum radius for the OML regime to hold).

2 Straight lines in the E (energy) vs J^2 (squared angular momentum) plane, for the r-family defined in Eq.(10), $J^2 = J_r^2(E)$. Shown are r-lines for the probe and for Fig.1 points 0, 1 and m [where $r^2\Phi(r)$ is maximum], as well as the envelope of lines in the r_0-r_1 range.

1

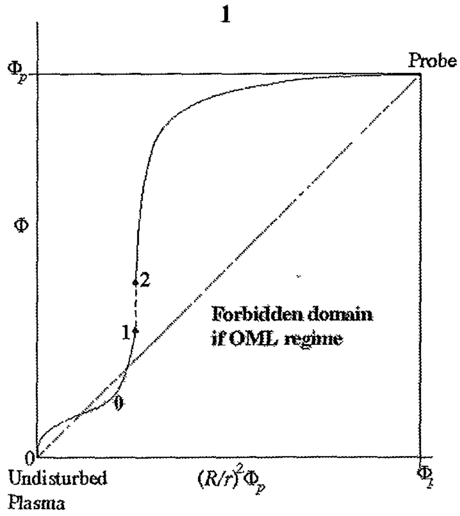

2